

ARTICLE OPEN

Deterministic bidirectional communication and remote entanglement generation between superconducting qubits

N. Leung¹, Y. Lu¹, S. Chakram¹, R. K. Naik¹, N. Earnest¹, R. Ma¹, K. Jacobs^{2,3}, A. N. Cleland⁴ and D. I. Schuster¹

We propose and experimentally demonstrate an efficient scheme for bidirectional and deterministic photonic communication between two remote superconducting modules. The two chips, each consists of a transmon, are connected through a one-meter long coaxial cable that is coupled to a dedicated “communication” resonator on each chip. The two communication resonators hybridize with a mode of the cable to form a dark “communication mode” that is highly immune to decay in the coaxial cable. We overcome the various restrictions of quantum communication channels established by other recent approaches in deterministic communication for superconducting qubits. Our approach enables bidirectional communication, and eliminates the high insertion loss and large volume footprint of circulators. We modulate the transmon frequency via a parametric drive to generate sideband interactions between the transmon and the communication mode. We demonstrate bidirectional single-photon transfer with a success probability exceeding 60%, and generate an entangled Bell pair with a fidelity of $79.3 \pm 0.3\%$.

npj Quantum Information (2019)5:18; <https://doi.org/10.1038/s41534-019-0128-0>

INTRODUCTION

A practical quantum computer requires a large number of qubits working in cooperation,¹ a challenging task for any quantum hardware platform. For superconducting qubits, there is an ongoing effort to integrate increasing numbers of qubits on a single chip.^{2–8} A promising approach to scaling up superconducting quantum computing hardware is to adopt a modular architecture^{9–11} in which modules are connected together via communication channels to form a quantum network. This reduces the number of qubits required on a single chip, and allows greater flexibility in reconfiguring and extending the resulting information processing system. In such an architecture, each module is capable of performing universal operations on multiple-bits, and neighboring modules are connected through photonic channels, allowing communication and entanglement generation between remote modules.

Remote entanglement between superconducting qubits has been realized probabilistically.^{12–14} A deterministic quantum communication channel is advantageous over a probabilistic one because it lowers the threshold requirement for fault-tolerant quantum computation and can achieve higher entanglement rates.¹⁵ Realizing deterministic photonic communication requires releasing a single photon from one qubit and catching it with the remote qubit. In the long-distance limit, the photon emission and absorption are from a continuum density of states. In this limit, static coupling limits the maximum transfer fidelity to only 54%.^{16,17} This limit is exceeded by dynamically tailoring the emission and absorption profiles.^{18–21} These capabilities are presently being used to perform photonic communication between superconducting qubits connected by a transmission line within a cryostat.^{14,22–24} In these experiments, the use of a

circulator enables the finite-length transmission line to be modeled as a long line with a continuum density of states, at the cost of added transmission loss.

Here, we establish bidirectional photonic communication between two superconducting qubits through a multimodal communication channel. Rather than inserting a circulator, the multimode nature of the finite length transmission line is made manifest and exploited.²⁵ For intra-cryostat communication, the required connection coaxial cable length of 1 m or less results in a free spectral range on the order of hundreds of MHz. In this setting, the resonances of the coaxial cable form hybridized normal modes with on-chip communication resonators, and photons are transferred coherently through the discrete modes of the channel in contrast to emission/absorption through a continuum. We use parametric flux modulation of the qubit frequency to generate resonant sideband interactions between the qubit and the communication channel.^{26–30} This approach avoids the loss due to the circulator that significantly limits the communication fidelity, and enables bidirectional quantum communication. Moreover, avoiding large volume footprint circulators facilitates the establishment of communication channels between multiple devices within a cryostat.

RESULTS AND DISCUSSION

Bidirectional communication

To demonstrate photonic communication between the two chips, we send a single photon from one chip to the other. First, we excite the sender qubit, then we switch on sideband interactions simultaneously on both qubits, targeting the communication channel. This effectively creates a Λ -system between single

¹The James Franck Institute and Department of Physics, University of Chicago, Chicago, IL 60637, USA; ²U.S. Army Research Laboratory, Computational and Information Sciences Directorate, Adelphi, MD 20783, USA; ³Department of Physics, University of Massachusetts at Boston, Boston, MA 02125, USA and ⁴Institute for Molecular Engineering, University of Chicago, Chicago, IL 60637, USA

Correspondence: N. Leung (nelsonleung@uchicago.edu) or Y. Lu (luy100@uchicago.edu)

These authors contributed equally: N. Leung, Y. Lu

Received: 16 August 2018 Accepted: 3 January 2019

Published online: 15 February 2019

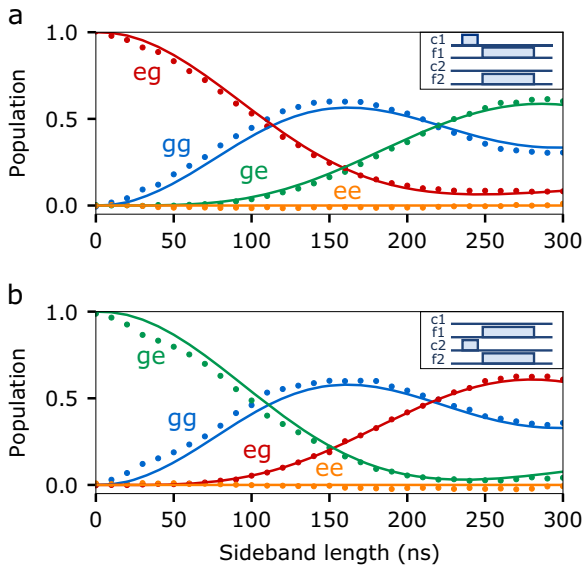


Fig. 1 Bidirectional excitation transfer. The inset at top right shows the pulse sequence used to implement excitation transfer. The labels $c1$, $c2$ denote the charge drives on qubits 1 and 2, respectively, and $f1$, $f2$ the respective flux drives. We first apply a π pulse to excite one of the qubits, then simultaneously switch on the sideband flux pulse to drive the transfer process. Using the same sideband sequence, but instead applying the π pulse to the other qubit, we can send a single photon in the opposite direction. The transfer fidelity is limited by qubit dephasing and photon decay in the communication mode. Described in the following, the transfer process in different directions have slightly different loss mechanisms. **a** Excitation transfer from qubit 1 to qubit 2. Notice that in this transfer process the sender qubit is not able to fully release its excitation (population of $|eg\rangle$ does not reach zero). As confirmed by the master equation simulation, this is due to the dephasing of qubit 1. The remaining errors arise from communication cavity loss and dephasing of qubit 2, which is less than that of qubit 1. **b** Excitation transfer from qubit 2 to qubit 1. In this process, while qubit 2 releases most of its excitations (population of $|ge\rangle$ comes close to zero), the dephasing of qubit 1 prevents it from capturing all the excitations in the communication mode, resulting in a slightly higher final population in $|gg\rangle$. The resulting fidelities for the transfer in the two directions are similar: $\{P_{|ge\rangle}, P_{|eg\rangle}\} \approx 61\%$, confirming the results from our numerical simulation

photon states of the qubits and the communication mode. We send a photon in the reverse direction using the same sideband sequence but instead exciting the other qubit, thus demonstrating bidirectional photon transfer. Figure 1 shows the transmon population plotted as a function of the sideband pulse length. The master equation simulation results (solid lines) are shown along with the experimental data (dots). We are able to obtain photon transfer with a success rate of $\{P_{|ge\rangle}, P_{|eg\rangle}\} \approx 61\%$. We use simultaneous square pulses for the time-envelopes of the sideband interactions. From the simulations detailed in the appendix, we found that square pulses gave superior performance for our current circuit parameters. Note that the achieved transfer fidelity exceeds 54%, the maximum fidelity for absorbing a naturally shaped emission into a continuum.^{16,17} This demonstrates a qualitative difference in transferring via a multimode cable compared to that of releasing and catching flying photonic qubits through a continuum.

The transfer fidelity is limited by qubit dephasing and photon decay in the communication mode. Qubit 1 has a higher dephasing rate ($T_2^* \approx 700$ ns) than qubit 2 ($T_2^* \approx 1.4$ μ s). The dephasing rate of qubit 1 is comparable to the sideband coupling rate, with the result that this qubit is not able to fully release its excitation during the transfer process. Conversely, for transfer in

the other direction qubit 1 is not able to receive all of the excitations. This transfer infidelity can be largely mitigated by using a fixed-frequency qubit less susceptible to the flux noise, with its coupling strength to the communication mode parametrically controlled via a tunable coupler circuit.^{29–33} The remaining loss of transfer fidelity comes from the loss in the communication mode. From our numerical simulations detailed in the appendix, we estimate that the overall photon loss in both the qubits and the communication mode contribute to an infidelity of 24%, while the dephasing error of the two qubits accounts for an infidelity of 15%. The sideband coupling rate of the transmon is limited by the range over which its frequency can be parametrically tuned, resulting in a maximum effective sideband coupling to the communication resonator of ≈ 2 MHz. With improved qubit coherence time, our simulation shows that more sophisticated transfer protocols such as STIRAP^{34,35} can be employed to boost transfer efficiency.

Bell state entanglement

We now entangle two qubits by creating a Bell state between the transmons on the respective chips.³⁶ We can create such a state by first applying the \sqrt{i} SWAP gate between the excited qubit 1 and the communication mode, which generates the Bell state $(|g1\rangle + |e0\rangle)/\sqrt{2}$ between them. We implement the \sqrt{i} SWAP by applying a sideband modulation pulse to qubit 1 to perform a $\pi/2$ rotation. Subsequently, we transfer the state of the communication mode to qubit 2 through the i SWAP gate by applying a sideband modulation pulse to the latter to perform a π rotation. Ideally this sequence prepares the Bell state $|\Psi^+\rangle = (|ge\rangle + |eg\rangle)/\sqrt{2}$ shared between the two remote qubits. To minimize decoherence the sender and receiver pulses can be applied simultaneously, so long as the lengths and amplitudes of the pulses are adjusted appropriately. Choosing qubit 1 as the sender and using square pulses, we found—both in our simulation and in the experiment—that maximal fidelity was obtained by setting both pulses at the same coupling rate and the length of the receiver pulse to be slightly longer than twice that of the sender, demonstrated by the pulse sequence diagram in Fig. 2b. The resulting Bell state has a fidelity of $\langle \Psi^+ | \rho_{\text{exp}} | \Psi^+ \rangle = 79.3 \pm 0.3\%$. We obtained the density matrix ρ_{exp} using quantum state tomography with an over-complete set of measurements complemented with the maximum likelihood method,³⁷ and we corrected the measurement error by constructing a confusion matrix (detailed in the appendix). It can be inferred from the data that the fidelity is almost equally limited by photon decay in the cable and the qubit dephasing errors. We also note that the Bell state fidelity is significantly higher than the success probability we achieved for photon transfer. This is because the superposition state that is transferred has less participation in the communication mode which is the primary source of loss. The dephasing losses on both qubits are also reduced due to either shorter interaction time or lower average excitations.

METHODS

Photonic communication by parametric interaction

Each chip consists of a single flux-tunable transmon and two additional resonators.³⁸ The first of these resonators is used for readout, and the second is coupled to the coaxial cable to enable the inter-module communication. The transmon can resonantly couple to the communication resonator through parametric flux modulation to realize inter-module photonic communications. Figure 3 shows a schematic of our two modules. The readout resonators have frequencies [module 1: 5.7463 GHz; module 2: 5.7405 GHz], and the communication resonators have frequencies [≈ 7.88 GHz, see the appendix for detailed analysis of parameters]. We operate the transmons at the static frequency of [1: 4.7685 GHz; 2: 4.7420 GHz] with an anharmonicity of [1: 109.8 MHz; 2: 109.9 MHz]. Each chip also has an eight-bit quantum memory³⁹ with

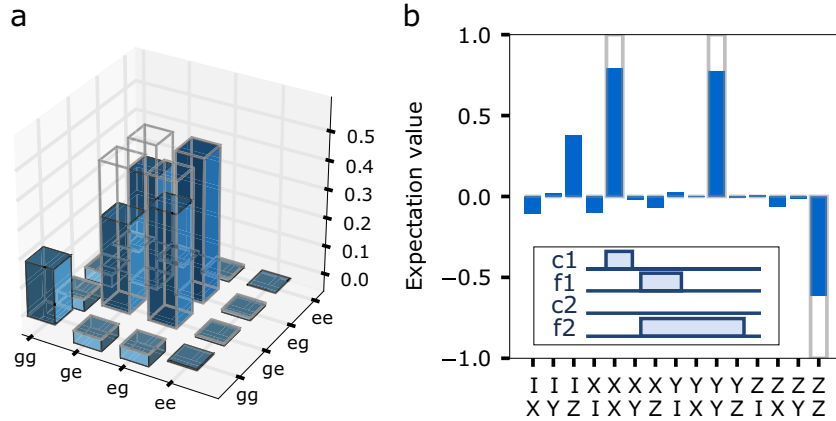


Fig. 2 Bell pair creation. **a** Real component of the density matrix. **b** Expectation values of two-qubit Pauli operators. We create a Bell state between two remote qubits, one on each module. This is achieved by first applying the \sqrt{i} SWAP gate between the excited qubit 1 and the communication mode, which is implemented by a sideband modulation pulse to qubit 1 to perform a $\pi/2$ rotation. A similar pulse, this time a π rotation, applied to the second qubit performs an i SWAP that transfers the entanglement from the communication mode to the second qubit. As shown in the inset, we implement the two pulses simultaneously to reduce decoherence. We obtain the resulting Bell state with fidelity $\langle \Psi^+ | \rho_{\text{exp}} | \Psi^+ \rangle = 79.3 \pm 0.3\%$

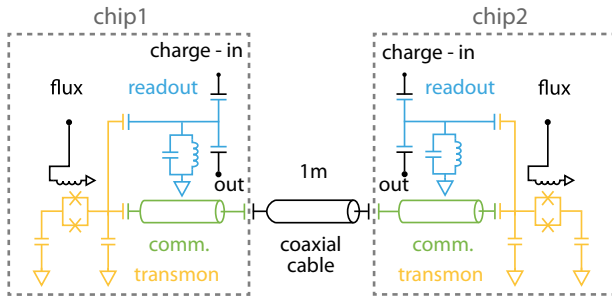


Fig. 3 Device circuit diagram. Each chip consists of a frequency-tunable transmon, a resonator included for readout, and a second resonator coupled to the coaxial cable (~ 1 m) that provides the communication link between the chips. The cable we used is a Tinned Hand-formable Microwave Cable (UT-085C-Form) with the silver-plated copper wire. The two communication resonators are designed to have identical frequencies. They are chosen to be coplanar waveguide resonators with a large center pin and gap width to make the frequency insensitive to fabrication variations.⁴¹ The simple circuit diagram shows the circuit model of each module. We induce resonant interactions between the transmon and the communication mode by modulating the transmon frequency via its flux bias at the frequency difference (detuning) between the mode and the transmon

eigenmode frequencies spanning from 5.8 to 7.7 GHz. These quantum memory modes can be utilized for universal quantum computation on each module locally but are not used in this work.

We induce resonant interactions between the transmon and the communication channel by modulating the transmon frequency via its flux bias. The modulation creates sidebands of the transmon excited state, detuned from the original resonance by the frequency of the applied flux tone. When one of these sidebands is resonant with a mode, the system experiences stimulated vacuum Rabi oscillations.³⁹ This process is similar to resonant vacuum Rabi oscillations,⁴⁰ but occur at a rate that is controlled by the modulation amplitude.^{27,28} To illustrate the application of parametric control, we employ the following experimental sequence. First, the transmon is excited via its charge bias. Subsequently, we modulate the flux bias to create sidebands of the transmon excited state at the modulation frequency. This is repeated for different flux pulse durations and frequencies, with the population of the transmon excited state measured at the end of each sequence. When the frequency matches the detuning between the transmon and a given eigenmode, we observe full-contrast stimulated vacuum Rabi oscillations. Figure 4 shows that the transmon can selectively interact with each of the eigenmodes of the

communication channel by choosing the appropriate modulation frequency. The photon transfer process between two remote qubits is initiated by switching on the sideband interactions targeting the communication resonator on each chip. As the bare frequencies of the transmon and the communication resonator are far detuned ($\Delta \approx 3$ GHz, $g \approx 50$ MHz), the sideband coupling scheme for photonic communication achieves a high on/off ratio. The following section explain the details of the multimode nature of our communication channel.

Multimode communication channel

The two communication resonators are designed to have identical frequencies. They are chosen to be coplanar waveguide resonators with a large center pin and gap width to make the frequency insensitive to fabrication variations.⁴¹ These resonators are coupled via the one-meter long coaxial cable, where the cable can be thought of as a multimode resonator with a free spectral range of around 100 MHz. The coupling strength between the cable and the communication resonators is $g_c \approx 7$ MHz. The cable mode that we use for communication has a frequency that is within g_c of the frequencies of the communication modes. Since the free spectral range of the coaxial cable is an order of magnitude larger than g_c , we consider the cable as a single mode nearly resonant with the communication resonators. The cable and the communication resonators thus together produce three hybridized normal modes which are depicted in Fig. 4. The near-degeneracy of the coaxial cable with the two communication resonators give rise to this almost equally-spaced three-mode structure, which can be seen from the three stimulated vacuum Rabi chevrons in Fig. 4b. The center normal mode used for communication ideally has no participation in the cable mode, and as a result, its loss rate is limited by the internal quality factors of the communication resonators and small Purcell losses from neighboring cable modes. The transfer fidelity is ultimately limited by the single pass loss of the cable (see Appendix). In comparison to the neighboring modes, the center normal mode couples more strongly to both qubits due to higher wavefunction participation at the communication resonators. Thus, this communication mode has both the advantages of high-quality factor and high coupling rate. For any practical device, the center normal mode does have a non-zero participation in the lossy coaxial cable due to a frequency mismatch between the two on-chip communication resonators. For our device, we found this frequency mismatch to be 5 MHz (detailed in the appendix), resulting in a less than 7% of cable mode participation in the communication mode.

The coherence time of the communication mode can be characterized using protocols analogous to those for the transmon. For instance, for mode T_1 one would first excite the transmon, then apply an i SWAP to transfer the excitation to the mode. After some variable time, another i SWAP is applied to transfer the excitation back to the transmon and we measure the transmon state subsequently.³⁹ We find $T_1 = 550$ ns and $T_2^* = 1 \mu$ s, corresponding to a quality factor of about 27,000. This quality factor is

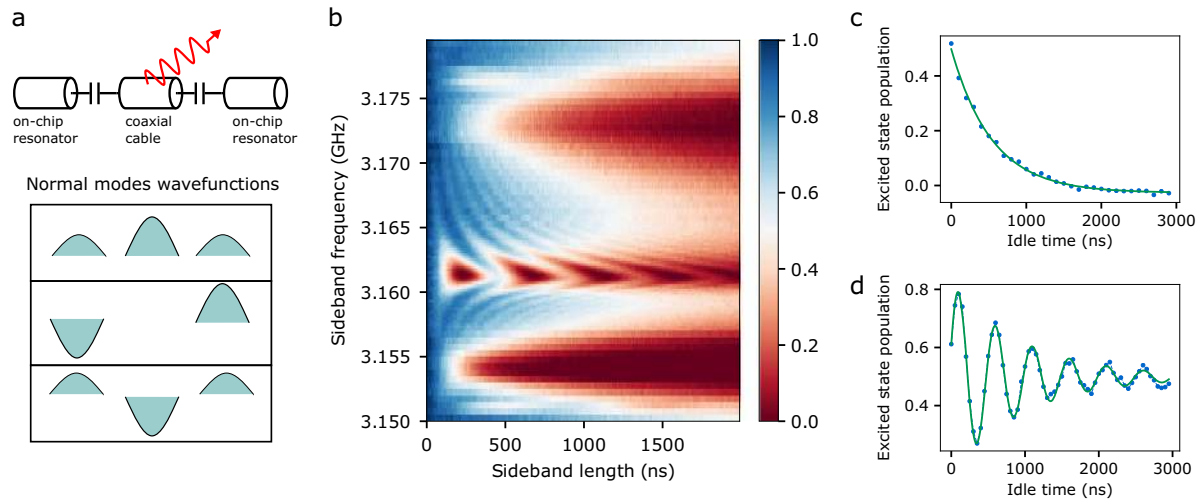


Fig. 4 Hybridized normal modes. **a** The schematic showing the wavefunctions of the coupled system involving the communication resonators and the coaxial cable. The three degenerate modes hybridize and form three normal modes with distinct signatures. The center normal mode has minimal participation in the lossy cable mode and has high-quality factor. **b** Stimulated vacuum Rabi oscillations around the communication modes. The near-degeneracy of the coaxial cable with the two communication resonators give rise to this almost equally-spaced three-mode structure. Being the two bright modes that include the lossy cable mode, and the dark “communication” mode of the two resonators. The latter couples more strongly to both qubits, and has a lifetime that is ideally only limited by the internal quality factors of the communication resonators. By fitting the simulation to experimental data, we found that the coaxial cable has a slightly higher frequency than the on-chip communication resonators [see Appendix]. **c**, **d** T_1 and T_2^* data of the communication mode. The coherence time of the communication mode is characterized through protocols analogous to those for the transmon. We characterize both T_1 and T_2^* of the communication mode, and find $T_1 = 550$ ns and $T_2^* = 1$ μ s

reasonably high, considering that it involves losses from the long lossy cable, wirebonds, solder of the SMA connector, and the copper leads of the sample holder. The two neighboring normal modes have much lower coherence times due to the higher participation of the lossy cable mode. From fitting to Fig. 4b we estimate the T_1 for the bare communication resonator and the bare cable mode to be ~ 5 μ s and ~ 40 ns, respectively (see Appendix). The dark state communication mode explored in this work can thus be utilized to improve transfer efficiency. In the following, we demonstrate the use of the dark state communication mode for bidirectional photon transfer and Bell-state generation.

We have realized photonic communication between two remote modules, a first step in realizing a modular network. The sideband modulation of the transmon qubit in each module can be applied to implement local operations on the multimode resonators and to perform photon transfer between the two modules. The multimode characteristic of the communication channel (a coaxial cable) is enabled by the absence of a circulator. This mode structure results in normal modes that are superpositions of a mode of the inter-module communication cable and the on-chip resonators. One of these normal modes is “dark” to the coaxial cable mode, thus avoiding much of the cable loss and allowing for high fidelity photon transfer. We characterized our system by performing single photon transfer with 61% fidelity and Bell-state preparation with 79.3% fidelity. These fidelities can be increased by improving the qubit coherence time and the strength of the coupling to the communication channel. This work sets the stage for future exploration in high fidelity and scalable quantum communications. Fidelity can be further improved by implementing more sophisticated photon transfer protocols (e.g., STIRAP). Another exciting direction is scaling to multiple communication channels on the same cable, and exploring the crossover between distributed modes and the continuum as the cable gets longer. Finally, one can employ heralding^{42,43} and exploit the ability to perform high fidelity local gates in conjunction with photonic communication to distill entanglement^{44–46} or perform forward error correction.⁴⁷

DATA AVAILABILITY

Data available on request from authors.

ACKNOWLEDGEMENTS

The authors thank R. Cook, Y. Zhong, and A.A. Clerk for useful discussions, and A. Oriani for support with cryogenic facilities. This material is based upon work

supported by the Army Research Office under (W911NF-15-2-0058). The views and conclusions contained in this document are those of the authors and should not be interpreted as representing the official policies, either expressed or implied, of the Army Research Laboratory or the U.S. Government. The U.S. Government is authorized to reproduce and distribute reprints for Government purposes notwithstanding any copyright notation herein. Research was also supported by the U. S. Department of Defense under DOD contract H98230-15-C0453. This work was partially supported by the University of Chicago Materials Research Science and Engineering Center, which is funded by the National Science Foundation under Award No. DMR-1420709. This work made use of the Pritzker Nanofabrication Facility of the Institute for Molecular Engineering at the University of Chicago, which receives support from SHyNE, a node of the National Science Foundation’s National Nanotechnology Coordinated Infrastructure (NSF NNCI-1542205). We gratefully acknowledge support from the David and Lucile Packard Foundation.

AUTHOR CONTRIBUTIONS

N.L. and Y.L. contributed equally to this work. N.L. and Y.L. designed and fabricated the device, designed the experimental protocols, performed the experiments, and analyzed the data. K.J. provided theoretical support. S.C., R.N., N.E. and R.M. provided fabrication and experimental support. All authors co-wrote the paper.

ADDITIONAL INFORMATION

Supplementary information accompanies the paper on the *npj Quantum Information* website (<https://doi.org/10.1038/s41534-019-0128-0>).

Competing interests: The authors declare no competing interests.

Publisher’s note: Springer Nature remains neutral with regard to jurisdictional claims in published maps and institutional affiliations.

REFERENCES

- Fowler, A. G., Mariantoni, M., Martinis, J. M. & Cleland, A. N. Surface codes: Towards practical large-scale quantum computation. *Phys. Rev. A* **86**, 032324 (2012).
- Noroozian, O., Day, P. K., Eom, B. H., Leduc, H. G. & Zmuidzinas, J. Crosstalk reduction for superconducting microwave resonator arrays. *Ieee. Trans. Microw. Theory Tech.* **60**, 1235–1243 (2012).

3. Wenner, J. et al. Wirebond crosstalk and cavity modes in large chip mounts for superconducting qubits. *Supercond. Sci. Technol.* **24**, 065001 (2011).
4. Chen, Z. et al. Fabrication and characterization of aluminum airbridges for superconducting microwave circuits. *Appl. Phys. Lett.* **104**, 052602 (2014).
5. Vesterinen, V., Saira, O. P., Bruno, A. & DiCarlo, L. Mitigating information leakage in a crowded spectrum of weakly anharmonic qubits, <http://arxiv.org/abs/1405.0450> (2014).
6. Foxen, B. et al. Qubit compatible superconducting interconnects, <http://arxiv.org/abs/1708.04270> (2017).
7. Dunsworth, A. et al. A method for building low loss multi-layer wiring for superconducting microwave devices. *Appl. Phys. Lett.* **112**, 063502 (2018).
8. Rosenberg, D. et al. 3D integrated superconducting qubits. *npj Quantum Inf.* **3**, 42 (2017).
9. Monroe, C. et al. Large-scale modular quantum-computer architecture with atomic memory and photonic interconnects. *Phys. Rev. A* **89**, 022317 (2014).
10. Brecht, T. et al. Multilayer microwave integrated quantum circuits for scalable quantum computing. *npj Quantum Inf.* **2**, 16002 (2016).
11. Chou, K. S. et al. Deterministic teleportation of a quantum gate between two logical qubits, <http://arxiv.org/abs/1801.05283> (2018).
12. Roch, N. et al. Observation of measurement-induced entanglement and quantum trajectories of remote superconducting qubits. *Phys. Rev. Lett.* **112**, 170501 (2014).
13. Narla, A. et al. Robust concurrent remote entanglement between two superconducting qubits. *Phys. Rev. X* **6**, 031036 (2016).
14. Dickel, C. et al. Chip-to-chip entanglement of transmon qubits using engineered measurement fields. *Phys. Rev. B* **97**, 064508 (2018).
15. Jiang, L., Taylor, J. M., Sørensen, A. S. & Lukin, M. D. Distributed quantum computation based on small quantum registers. *Phys. Rev. A* **76**, 062323 (2007).
16. Stobińska, M., Alber, G. & Leuchs, G. Perfect excitation of a matter qubit by a single photon in free space. *EPL (Europhys. Lett.)* **86**, 14007 (2009).
17. Wang, Y., Minář, J., Sheridan, L. & Scarani, V. Efficient excitation of a two-level atom by a single photon in a propagating mode. *Phys. Rev. A* **83**, 063842 (2011).
18. Yin, Y. et al. Catch and release of microwave photon states. *Phys. Rev. Lett.* **110**, 107001 (2013).
19. Srinivasan, S. J. et al. Time-reversal symmetrization of spontaneous emission for quantum state transfer. *Phys. Rev. A* **89**, 033857 (2014).
20. Pechal, M. et al. Microwave-controlled generation of shaped single photons in circuit quantum electrodynamics. *Phys. Rev. X* **4**, 041010 (2014).
21. Wenner, J. et al. Catching time-reversed microwave coherent state photons with 99.4% absorption efficiency. *Phys. Rev. Lett.* **112**, 210501 (2014).
22. Axline, C. J. et al. On-demand quantum state transfer and entanglement between remote microwave cavity memories. *Nat. Physics* **14**, 705–710 (2018).
23. Campagne-Ibarcq, P. et al. Deterministic Remote Entanglement of Superconducting Circuits through Microwave Two-Photon Transitions. *Phys. Rev. Lett.* **120**, 200501 (2018).
24. Kurpiers, P. et al. Deterministic quantum state transfer and remote entanglement using microwave photons. *Nature* **558**, 264–267 (2018).
25. Jacobs, K. et al. Fast quantum communication in linear networks. *EPL (Europhys. Lett.)* **114**, 40007 (2016).
26. Leek, P. et al. Using sideband transitions for two-qubit operations in superconducting circuits. *Phys. Rev. B* **79**, 180511 (2009).
27. Beauvain, F., da Silva, M. P., Dutton, Z. & Blais, A. First-order sidebands in circuit QED using qubit frequency modulation. *Phys. Rev. A* **86**, 022305 (2012).
28. Strand, J. D. et al. First-order sideband transitions with flux-driven asymmetric transmon qubits. *Phys. Rev. B* **87**, 220505 (2013).
29. Sirois, A. J. et al. Coherent-state storage and retrieval between superconducting cavities using parametric frequency conversion. *Appl. Phys. Lett.* **106**, 172603 (2015).
30. McKay, D. C. et al. Universal Gate for Fixed-Frequency Qubits via a Tunable Bus. *Phys. Rev. Appl.* **6**, 064007 (2016).
31. Allman, M. et al. Tunable resonant and nonresonant interactions between a phase qubit and 1 c resonator. *Phys. Rev. Lett.* **112**, 123601 (2014).
32. Chen, Y. et al. Qubit architecture with high coherence and fast tunable coupling. *Phys. Rev. Lett.* **113**, 220502 (2014).
33. Lu, Y. et al. Universal stabilization of a parametrically coupled qubit. *Phys. Rev. Lett.* **119**, 150502 (2017).
34. Halfmann, T. & Bergmann, K. Coherent population transfer and dark resonances in SO₂. *J. Chem. Phys.* **104**, 7068 (1998).
35. Vasilev, G. S., Kuhn, A. & Vitanov, N. V. Optimum pulse shapes for stimulated Raman adiabatic passage. *Phys. Rev. A* **80**, 013417 (2009).
36. Bell, J. On the einstein-podolsky-rosen paradox. *Physics* **1**, 195–200 (1964).
37. James, D. F. V., Kwiat, P. G., Munro, W. J. & White, A. G. Measurement of qubits. *Phys. Rev. A* **64**, 052312 (2001).
38. McKay, D. C., Naik, R., Reinhold, P., Bishop, L. S. & Schuster, D. I. High-contrast qubit interactions using multimode cavity QED. *Phys. Rev. Lett.* **114**, 080501 (2015).
39. Naik, R. K. et al. Random access quantum information processors using multimode circuit quantum electrodynamics. *Nat. Commun.* **8**, 1904 (2017).
40. Rempe, G., Walther, H. & Klein, N. Observation of quantum collapse and revival in a one-atom maser. *Phys. Rev. Lett.* **58**, 353–356 (1987).
41. Underwood, D. L., Shanks, W. E., Koch, J. & Houck, A. A. Low-disorder microwave cavity lattices for quantum simulation with photons. *Phys. Rev. A* **86**, <https://journals.aps.org/pra/pdf/10.1103/PhysRevA.86.023837> (2012).
42. Azuma, K., Tamaki, K. & Lo, H.-K. All-photonic quantum repeaters. *Nat. Commun.* **6**, 6787 (2015).
43. Mosley, P. J. et al. Heralded generation of ultrafast single photons in pure quantum states. *Phys. Rev. Lett.* **100**, 133601 (2008).
44. Kwiat, P. G., Barraza-Lopez, S., Stefanov, A. & Gisin, N. Experimental entanglement distillation and ‘hidden’ non-locality. *Nature* **409**, 1014 (2001).
45. Takahashi, H. et al. Entanglement distillation from gaussian input states. *Nat. Photonics* **4**, 178 (2010).
46. Dong, R. et al. Experimental entanglement distillation of mesoscopic quantum states. *Nat. Phys.* **4**, 919 (2008).
47. Mohr, A. E., Riskin, E. A. & Ladner, R. E. Unequal loss protection: Graceful degradation of image quality over packet erasure channels through forward error correction. *IEEE J. Sel. Areas Commun.* **18**, 819–828 (2000).



Open Access This article is licensed under a Creative Commons Attribution 4.0 International License, which permits use, sharing, adaptation, distribution and reproduction in any medium or format, as long as you give appropriate credit to the original author(s) and the source, provide a link to the Creative Commons license, and indicate if changes were made. The images or other third party material in this article are included in the article's Creative Commons license, unless indicated otherwise in a credit line to the material. If material is not included in the article's Creative Commons license and your intended use is not permitted by statutory regulation or exceeds the permitted use, you will need to obtain permission directly from the copyright holder. To view a copy of this license, visit <http://creativecommons.org/licenses/by/4.0/>.

© The Author(s) 2019